

LASER-INDUCED CAVITATION IN LIGHT-ABSORBING LIQUIDS

MARTIN H. KLEIN SCHAARSBERG

Bachelor thesis

BSc Advanced Technology
Physics of Fluids Group
Faculty of Science and Technology
University of Twente

24 June 2012

Martin H. Klein Schaarsberg: *Laser-induced cavitation in light-absorbing liquids*,
Bachelor thesis, BSc Advanced Technology, © 24 June 2012

BACHELOR ASSIGNMENT COMMITTEE:

Chairman · Prof. Dr. Detlef Lohse

Supervisor · Ir. Claas Willem Visser

External examiner · Prof. Dr. Miko Elwenspoek

Member · Dr. Chao Sun

CHAIR:

Physics of Fluids Group

Faculty of Science and Technology

University of Twente

LOCATION:

Enschede

TIME FRAME:

April–June 2012

ABSTRACT

This thesis presents an experimental and numerical study of laser-induced cavitation in capillary tubes. An experimental study of the influence of focal position of the laser reveals that cavitation bubble formation is enhanced when the laser focus is displaced from the capillary axis towards the laser. A numerical model based on a ray tracing method was developed to calculate the spatial energy absorption profile. Subsequently, a simple energy threshold model was used to obtain an estimation of the initial bubble volume. The estimation provides a good match with the experimentally observed trend and predicts an optimum position for the laser focus. The model may serve as a tool to optimize cavitation-based microfluidic systems, allowing study of the influence of the liquid absorptivity, the capillary diameter, the capillary wall thickness and the laser pulse energy and polarization on bubble formation. The local energy distribution, for which currently no adequate model exists, could also enhance the initial conditions of computational fluid dynamics models commonly used to describe cavitation dynamics.

CONTENTS

1	INTRODUCTION	1
2	EXPERIMENTAL WORK	3
2.1	Experimental setup	3
2.2	Results	4
2.3	Discussion & conclusion	7
3	NUMERICAL MODELLING OF LOCAL ENERGY ABSORPTION	9
3.1	Description of the ray tracing method	9
3.2	Discretization of a laser beam	10
3.3	Reflections & refractions	13
3.4	Spatial discretization of absorption	14
3.5	Estimation of bubble volume	15
4	EVALUATION OF THE NUMERICAL MODEL	17
4.1	Beam discretization convergence	17
4.2	Efficiency analysis	18
4.3	Results	19
4.4	Discussion & conclusion	21
5	CONCLUSIONS & RECOMMENDATIONS	23
5.1	Experimental work	23
5.2	Numerical modelling	23
5.3	Results	23
5.4	Outlook	23
A	REFLECTIONS & REFRACTIONS ON CYLINDRICAL BODIES	25
A.1	Points of intersection	25
A.2	Direction of transmitted and reflected rays	25
A.3	Intensity of transmitted and reflected light	26
B	OVERVIEW OF MODEL INPUT & OUTPUT PARAMETERS	29
	BIBLIOGRAPHY	31
	ACKNOWLEDGMENTS	33

When a laser pulse is focused on a liquid, the energy absorption can cause rapid evaporation (Lauterborn, 1972) and even optical or thermal breakdown (Felix and Ellis, 1971; Byun and Kwak, 2004). The evaporation due to the intense energy deposit results in a cavitation bubble that violently expands and collapses. This can cause e.g. shock waves, rapid jets (Tagawa et al., 2012) and sonoluminescence (Brenner et al., 2002). The aggressive nature of laser-induced cavitation has found a broad range of applications, such as cell lysis, cell membrane poration and ocular surgery (Quinto-Su et al., 2009). In microfluidics, cavitation is used for pumping, mixing, switching and moving objects. Cavitation can hereby produce inertia-dominated flow even within the small dimensions of microfluidics (Ohl et al., 2009). A novel example is the creation of highly focused supersonic microjets (Tagawa et al., 2012). Due to their excellent controllability, high velocity and relatively low power requirements, these jets are an attractive option for needle-free drug injection (Mitragotri, 2006).

To study the dynamics of laser-induced cavitation, various experimental techniques have been employed. High-speed cameras have proved useful to study the evolution of bubbles in time (Lauterborn, 1972; Gonzalez-Avila et al., 2011) and particle image velocimetry was used to study the flow field induced by cavitation (Zwaan et al., 2007). In addition, various numerical methods were developed, such as kinetic and energy balance models (Byun and Kwak, 2004; Sun et al., 2009) and applications of the boundary element method (Yang and Prosperetti, 2008; Gonzalez-Avila et al., 2011).

A key uncertainty in the current numerical methods is the initial distribution of absorbed energy after the usually nanosecond-scale laser pulse, which determines ‘the initial shape of the cavitation bubble and its induced flow field’ (Lim et al., 2010). According to Byun and Kwak (2004), ‘[t]he laser energy transmitted to the focusing region may depend on the focal length of the lens employed, the focusing angle and aberration of the laser front.’

For example, the model from Sun et al. (2009) requires an initial temperature profile, which currently is ‘a matter of considerable uncertainty because we do not have sufficient information on the spatial distribution of the absorbed laser energy.’ Lim et al. (2010) demonstrated that the bubble shape and evolution could be modified by changing the spatial energy distribution of the laser. However, in their boundary element simulations, the initial bubble shapes were estimated, as no model for the local energy absorption was developed.

To obtain the spatial distribution of absorbed energy of a nanoseconds laser pulse, this research presents a numerical approach. A ray tracing method directly relates the energy distribution to the absorptivity of the liquid, the geometry of the system and the laser energy, focusing angle and position. This allows calculation of the initial bubble shape from the local energy dump, instead of the currently common assumptions of initially spherical bubbles or other shapes.

A similar ray tracing method was used to model the infrared heating of plastic bottles during their production (Bordival et al., 2010; Cosson et al., 2011) and infrared composite curing (Nakouzi et al., 2011). Previously, ray tracing was also

successfully applied to model the radiation absorption in fluid collectors for solar energy collection (Sokolov and Saltiel, 1981) and heliostat solar power plants (Garcia et al., 2008).

To study the dependence of the local energy dump on bubble formation, cavitation bubbles in a capillary filled with ink were imaged for varying positions of the focal point of a laser. Chapter 2 starts with an overview of the experimental setup and results. Subsequently, Chapter 3 presents the numerical method that was developed. In Chapter 4, the model is evaluated and compared with the experiments. Chapter 5 concludes the thesis with a summary and outlook.

To study the dependence of the initial energy distribution on cavitation bubble generation, this thesis focuses on the influence of the position of the focal point of a laser within or outside a capillary tube filled with ink. This chapter describes the experiments performed to determine this influence.

2.1 EXPERIMENTAL SETUP

Figure 2.1 depicts the setup that was used to study the cavitation bubbles, similar to that of Sun et al. (2009) and Tagawa et al. (2012). A borosilicate glass capillary tube (Capillary Tube Supplies Limited) with an inner and outer diameter of respectively 200 and 220 μm was filled with ink by connecting one end to a syringe pump (*Harvard Apparatus PHD 2000*). The other end was left open to air. To create cavitation bubbles, a 7 ns laser pulse (Q-switched Nd-YAG laser, *Quantel Evergreen 70, version A*) was focused on a point on or outside the capillary using a beam expander (*Edmund Optics F64-418*) and a 10 \times microscope objective (*Thorlabs LMH-10X-532*). The laser's axis of propagation was aligned with the centre of the capillary by looking at its shadow on a detector card. To measure the pulse energy, half of the beam was diverted by a beam splitter towards an energy meter (*Gentec-EO QE12SP-S-MT-DO*) connected to an oscilloscope (*Tektronix TDS2014*). The bubbles in the capillary were imaged from the side with a high-speed camera (*PCO Sensicam*) connected to a 20 \times microscope objective (*Olympus system*). The camera recorded two frames for each experiment with an inter-frame delay of 2 ns. Exposure for the two frames was provided by laser induced fluorescence at 600–800 nm from a fluorescence box (*LaVision vZ11-5*) connected to two 7 ns pulsed lasers (532 nm Q-switched Nd-YAG lasers, *Litron Nano TRL 400-20 PIV*). Laser induced fluorescence reduces the laser coherence, which is undesirable for imaging purposes, while maintaining a nanoseconds pulse duration (van der Bos et al., 2011). To filter out remaining 532 nm radiation, a red filter was installed before the camera. The injection laser, exposure lasers and camera were triggered by a pulse/delay generator (*Berkeley Nucleonics, Model 555*).

The ink (*R.C. Universal Magenta 08402*) was diluted to a 10% solution in water. The absorption coefficient of the ink was determined using the Lambert–Beer law, which is given by

$$\frac{I}{I_0} = 10^{-\alpha \ell}, \quad (2.1)$$

where I/I_0 is the ratio of transmitted to incident power, ℓ the optical length and α (units m^{-1}) the absorption coefficient. Using a 532 nm laser and varying the incident power, the absorption coefficient of the 10 % ink solution was measured at $(84 \pm 4) \times 10^2 \text{ m}^{-1}$. A mirror reflecting only the 532 nm radiation was used to prevent the detection of 1064 nm radiation, which is radiated by the sample as the ink acts as a wavelength modulator.

Imaging of bubbles was performed by M.S. Al, T.A.M van Dijk, M.H. Klein Schaarsberg and C.W. Visser in a one-week project. The absorption coefficient of the ink was measured by C.W. Visser. Image processing and analysis was performed by M.H. Klein Schaarsberg.

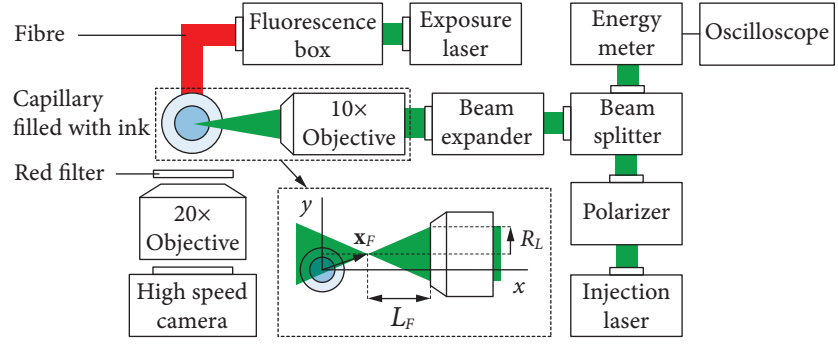


Figure 2.1: Experimental setup.

2.2 RESULTS

Figure 2.2 shows a range of typical images. Two images were recorded for every bubble, at $3 \mu\text{s}$ (Figure 2.2, top row) and $23 \mu\text{s}$ (bottom row) after an 8 mJ injection laser pulse. Every image pair from a–f belongs to a separate experiment. The focal displacement $= x_F \hat{e}_x + y_F \hat{e}_y$ is defined as the position of the projected focal point relative to the cylinder axis (inset of Figure 2.1). Here, \hat{e}_x is the unit vector in the direction perpendicular to the capillary axis and towards the laser, and \hat{e}_y is the unit vector in the direction perpendicular to \hat{e}_x and the capillary axis. In Figure 2.2a, the laser was approximately focused on the centre of the capillary ($x_F \approx 0$, $y_F \approx 0$). In subsequent images (e.g. Figure 2.2)b–f, the capillary was moved away from the laser, increasing the focal displacement x_F in steps.

2.2.1 Bubble volume

When the focal displacement is increased from in focus towards out focus, the bubble size increases (Figure 2.2a–c), as the laser presumably heats a larger volume of liquid. This trend will be investigated in Chapter 4 using the numerical model. As bubbles reach the capillary wall (Figure 2.2c–e), they continue to grow asymmetrically towards the open end of the capillary. If the displacement is increased even further, the bubble size declines again, as an increasing part of the laser beam exceeds the width of the capillary (Figure 2.2d–f).

To compare the experiments with simulations, an approximation of the bubble volume is required. A straightforward method is to determine the area of the bubble using image processing in MATLAB and to use this area to calculate the radius of a circle. With this radius, we can calculate the volume of a sphere. However, the more the bubble shape differs from a sphere, the more the calculated volume deviates from the real volume. For example, for a cylindrical bubble with a height twice the diameter, the volume is overestimated with 35 %.

A better approximation is given by the axisymmetric method. Here, the image is envisioned as a stack of disk-shaped slices viewed from the side. For bubbles that are not confined in a direction perpendicular to the laser beam, the best choice for the axis of symmetry is parallel to the laser axis, such as in Gonzalez-Avila et al. (2011). The bubble is then divided into vertical slices with thickness Δx of 1 pixel, such as in Figure 2.3a. In our case, this seems a good approach for small bubbles. However, as the bubbles grow and fill the capillary, this approach gives a

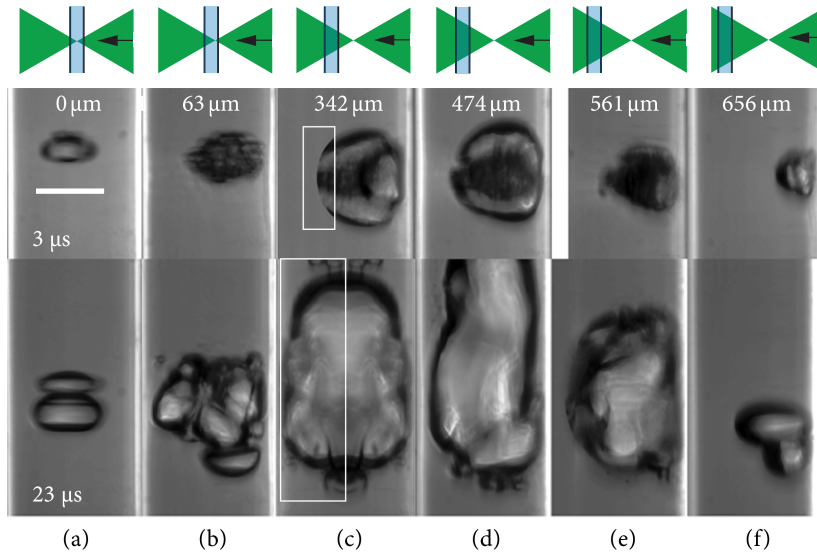


Figure 2.2: Variation of the bubble size and shape with focal displacement x_F in a side view of the capillary with the open end on top and the injection laser on the right. Each image has a width equal to the inner diameter of the capillary. The scale bar indicates a length of $100\ \mu\text{m}$ and the drawings above the pictures indicate the position of the laser beam, which is shown in realistic proportions to the capillary diameter.

great overestimation of the bubble volume, because the bubble shape approaches the shape of a cylinder (such as Sun et al. (2009)). Here, division in horizontal slices (with thickness Δz of 1 pixel) seems a better method (Figure 2.3b). To make a division between the two methods, we have chosen to use the direction in which the bubble is largest, horizontal or vertical, as the axis of symmetry.

Still, an overestimation of the bubble volume is likely due to the morphology of the bubbles. Instead of a solid body, the images show the formation of very small bubbles (Figure 2.2, top row), which merge into one or more bigger bubbles (Figure 2.2, bottom row). For a cloud of bubbles, such as in Figure 2.2b (top) an indication of the possible overestimation of the volume fraction may be given by the empty volume between close packed spheres, which is 26 %.

The bubble contours were determined with background subtraction, contrast enhancement and thresholding using image processing routines in MATLAB. The bubbles were assumed to consist of full circular slices only, any holes perpendicular to the axis of symmetry were filled (which explains the horizontal line at the bottom in the contour of Figure 2.3b). Where necessary, the bubble edges were darkened manually using photo editing software to improve edge detection.

The variation of the resulting approximated volume with increasing focal displacement is displayed in Figure 2.4a. The error bars indicate a 20 % error that aims to capture the uncertainty of the actual bubble shape.

An average volume expansion rate was calculated from the increase in volume between 0 and $3\ \mu\text{s}$ and between 3 and $23\ \mu\text{s}$ (Figure 2.4b). The bubbles expand most rapidly at a displacement between 300 and $500\ \mu\text{m}$. Here, both the instantaneous volume and the expansion rate reach a maximum.

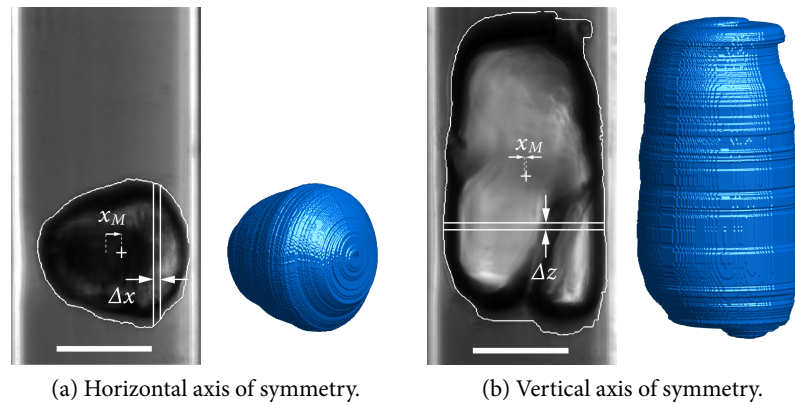


Figure 2.3: Side view of the capillary with an approximation of the bubble volume using the axisymmetric method. The scale bar indicates $100\ \mu\text{m}$ and the + indicates the centre of mass of the approximated volume.

The movement of the capillary between shots was measured with an error of $\pm 3\ \mu\text{m}$. However, the position of initial focal point in Figure 2.2a was measured with a much larger error of approximately $\pm 50\ \mu\text{m}$. Since all other positions are calculated relative to this point, each focal position subsequent to the initial focal position has an error of $\pm 54\ \mu\text{m}$. Nevertheless, the data provides sufficient information for qualitative analysis.

In 5 of 26 recorded images, a part of the bubble was not in the field of view of the camera. To use these bubbles in further approximate calculations, these bubbles were extrapolated, such as in the rectangles in Figure 2.2c. The data points obtained from these images are indicated by circles in Figure 2.4.

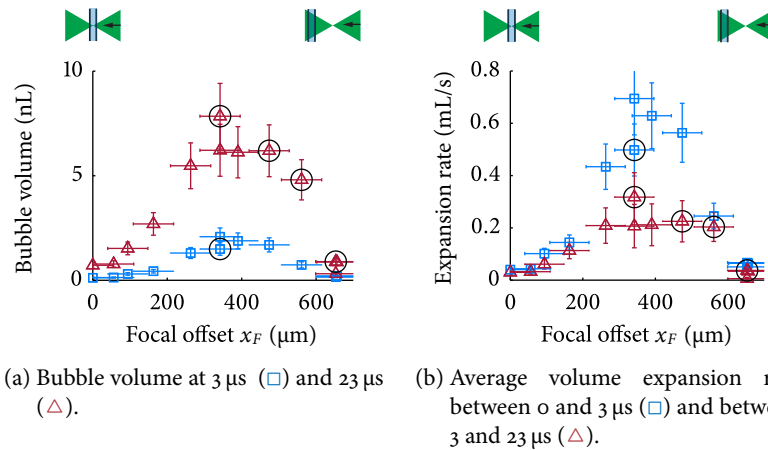


Figure 2.4: Development of bubble volume versus the relative focal displacement, for a $200\ \mu\text{m}$ capillary and $8\ \text{mJ}$ laser pulse. The circles indicate data from extrapolated images.

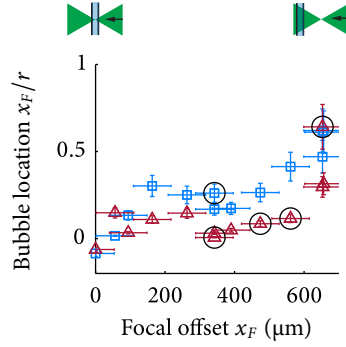


Figure 2.5: Position of the centre of mass of the bubble relative to the cylinder axis versus relative focal displacement at $3 \mu\text{m}$ (\square) and $23 \mu\text{m}$ (\triangle). The circles indicate data from extrapolated images.

2.2.2 Bubble location

To compare the position of the bubbles, the centre of mass of the approximated volume was calculated, assuming constant density. With the bubble volume approximated by N volume elements of unit mass, the distance of the centre of mass x_M from the capillary axis is given by the average of their positions x_i :

$$x_M = \frac{1}{N} \sum_i x_i. \quad (2.2)$$

Figure 2.5 shows how the imaged bubbles are located relative to the capillary axis as illustrated in Figure 2.3. The location x_M was non-dimensionalized by dividing by the inner capillary radius r (thus x_M/r is 0 at the capillary axis and 1 at the right edge of the capillary). For increasing focal displacement, the bubbles generally move closer to the capillary wall on the side of the laser. However, for a relative focal displacement of 300–500 μm , the bubbles move more towards the capillary axis. At the largest bubble volumes, where the bubble fills the entire cross-section of the capillary, the centre of mass is located on or near the capillary axis. Between $3 \mu\text{m}$ and $23 \mu\text{m}$, the bubbles grow and move towards the capillary axis.

2.3 DISCUSSION & CONCLUSION

High-speed imaging of laser-induced cavitation bubbles in a capillary tube for varying position of the focal point of the laser reveals that bubble expansion rate can be enhanced by placing the focal point at a distance from the capillary axis. This can be explained by a competition between two effects. The first effect is that the irradiance (power per area) in the cross-section of the beam decreases with distance for a diverging beam. If a threshold energy density is required for evaporation in a slice of cross-section of the beam, the evaporated part of this slice will decrease with distance. The other effect is that the volume that is initially irradiated by the laser increases as the focal point is moved away from the capillary axis. Before thermal diffusion and fluid dynamics come into play, bubble nucleation will not occur outside the volume where the beam strikes. The competition between the decrease of irradiance and the increase of heated

volume for increasing focal displacement explains the observed maximum in the bubble expansion rate ([Figure 2.4b](#)).

In the next chapter, the observed phenomena will be investigated further with a numerical model. The results of this model will be compared with the experimental results in [Chapter 4](#).

To improve the understanding of laser-induced cavitation, this chapter presents a numerical model for the local energy deposit. Numerical and experimental validation follows in [Chapter 4](#).

An analytical description of a laser beam requires a beam much smaller than the optical system ([Alda, 2003](#); [Greco and Giusfredi, 2007](#)). In our setup, the beam width can easily exceed the width of the capillary. For this reason, a ray tracing method was implemented to describe the interaction of the laser beam with the capillary, analogous to [Visser \(2011\)](#). This method is explained in [Section 3.1](#). As input, the laser beam and energy is discretized in a large number of infinitely thin rays ([Section 3.2](#)). [Section 3.3](#) explains the calculation of reflections and refractions. To model the local energy deposit, the liquid is assumed to satisfy the Lambert–Beer absorption equation. [Section 3.4](#) explains how the absorption is discretized in space with an algorithm by [Amanatides and Woo \(1987\)](#). [Section 3.5](#) concludes the chapter with a straightforward method to obtain an indication of the initial bubble volume from the modelled energy deposit.

3.1 DESCRIPTION OF THE RAY TRACING METHOD

[Figure 3.1](#) shows the result of the ray tracing method. First, the laser beam is divided into a large number of infinitely thin rays. Of these rays, the cascade of reflections and refractions of all the rays that intersect the capillary is calculated until a minimum intensity threshold is reached.

The initial radius of the beam modelled is taken equal to radius of the beam just before the lens. The specifications of the laser used in the experiments report a near-field beam diameter of 3.87 mm and 1.95 mrad divergence at 86.5%. With the setup's optical length of (1.31 ± 0.02) m, the divergence causes the beam radius to increase with 2.6 mm. Including the $3\times$ magnification of the beam expander, the final beam radius becomes 1.35 cm. Spherical aberration and diffraction effects are not taken into account. The finite beam waist that a Gaussian beam still has at the focal point is also neglected ([Alda \(2003\)](#)).

The starting points of all rays lie in a single yz -plane. The position of the starting point \mathbf{X}_0 of a ray at the centre of the beam is determined by the focal displacement \mathbf{x}_F and focal length L_F (see [Figure 2.1](#)):

$$\mathbf{X}_0 = L_F \hat{\mathbf{e}}_x + \mathbf{x}_F. \quad (3.1)$$

Each ray, with starting point \mathbf{X}_0 , is given a normalized direction vector \mathbf{v} towards the projected focal point:

$$\mathbf{v} = \frac{\mathbf{X}_0 - \mathbf{x}_F}{|\mathbf{X}_0 - \mathbf{x}_F|}. \quad (3.2)$$

The following section will explain the determination of the starting points of the rays and the energy per ray.

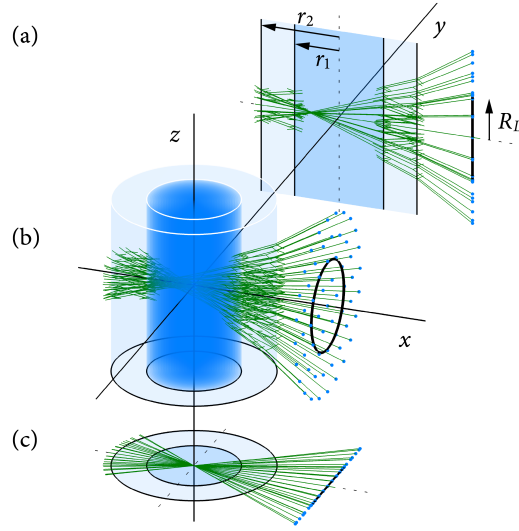


Figure 3.1: Ray tracing in a capillary tube. From top to bottom, (a), (b) and (c) show a side view, 3D view and top view of the traced rays. In the middle, the laser discretization in a regular pattern in the yz -plane is visible. The black line and ring on the right side indicate the beam radius R_L . The simulation started with 61 initial rays and ended with 613 rays.

3.2 DISCRETIZATION OF A LASER BEAM

A typical laser beam is characterized by a radial Gaussian irradiance profile,

$$I(r) = \frac{2P_t}{\pi R^2} \exp[-2(r/R)^2], \quad (3.3)$$

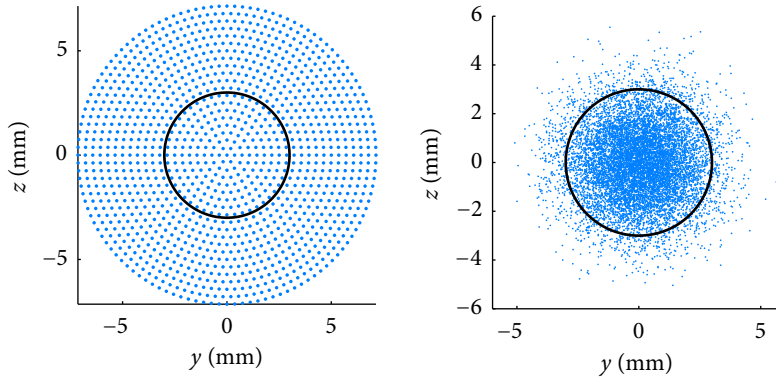
with r the distance from the beam centre, R the beam radius and P_t the total laser power. The beam radius can be interpreted as the distance from the beam axis where the irradiance has dropped to $1/e^2$. The prefactor ensures that the total laser power results if the irradiance is integrated over the entire cross-section of the beam:

$$P_t = \int_0^{2\pi} \int_0^\infty I(r)r dr d\theta. \quad (3.4)$$

To discretize the energy of the beam over the separate ray while maintaining a Gaussian irradiance profile, two methods were used. Figure 3.2a illustrates the first method, where the rays origins are distributed in a regular pattern with approximately equal area per ray. A Gaussian irradiance profile of the discretized beam is obtained by a proper distribution of energy per ray (Visser, 2011). The second method, illustrated in Figure 3.2b, uses a stochastic distribution for the ray origins with equal energy per ray. The two methods will be described in the following two sections.

3.2.1 Regular pattern beam discretization

Visser (2011) proposed to distribute the rays from the discretized beam in an approximately hexagonal pattern (Figure 3.2a). First, the power of the laser is



(a) Ray origins in a regular pattern with approximately equal area per ray with 20 rings, giving 1261 initial rays. Adapted from Visser (2011), with permission. (b) Ray origins in a stochastic pattern with Gaussian density and 10 000 initial rays.

Figure 3.2: Determination of ray origins for the discretization of a laser beam. The circles shows the beam radius R_L .

split over a centre ray at $r = 0$ and N annuli or rings (area between two concentric circles) around this first ray. Each annulus n has an inner radius $r_0(n)$ and an outer radius $r_1(n)$. To cover the whole laser beam, the outer and inner radii of consecutive annuli are equal ($r_1(n) = r_0(n+1)$). For the centre ray $r_0(0) = 0$, and for the outermost annulus, $r_1(N) = \infty$. Subsequently, each annulus is divided into $6n$ pieces, such that the area surrounding each ray centre is approximately equal. To determine the power for each ray in the n -th annulus, the irradiance $I(r)$ from (3.3) is integrated for each annulus and divided by the number of rays per annulus:

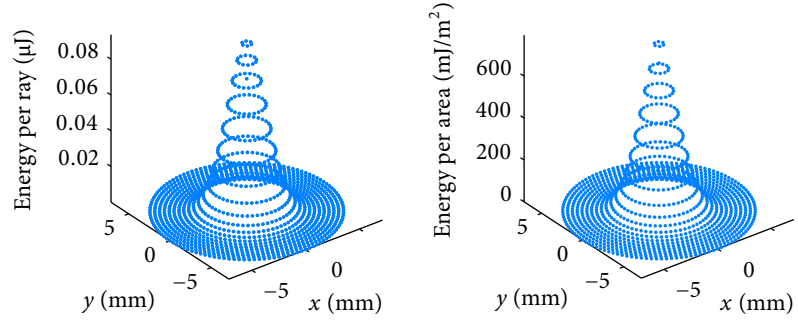
$$P(n) = \frac{1}{6n} \int_0^{2\pi} \int_{r_0(n)}^{r_1(n)} I(r) r dr d\theta \quad (3.5)$$

$$= \frac{P_t}{6n} \left\{ \exp[-2(r_0(n)/R)^2] - \exp[-2(r_1(n)/R)^2] \right\} \quad (3.6)$$

The 7 ns duration of the studied laser pulses is far shorter than the resulting dynamics. Therefore, we will consider each laser pulse as an instantaneous injection of energy from this point. It is then more convenient to use the total laser pulse energy $U_t = P_t T$ (with T the pulse duration) instead of power. This results in an energy per ray $U(n) = P(n) T$ (Figure 3.3a):

$$U(n) = \frac{U_t}{6n} \left\{ \exp[-2(r_0(n)/R)^2] - \exp[-2(r_1(n)/R)^2] \right\} \quad (3.7)$$

For the outermost annulus (at $2.5R$), the energy per ray is slightly higher, as the irradiance is integrated from $\approx 2.5R$ to infinity. This difference is negligible, however, since this last annulus contains only $\approx 0.2\%$ of the total beam energy. The resulting discretized irradiance profile (multiplied by the pulse duration to obtain the ratio of energy per ray to surface per ray) has a Gaussian distribution (Figure 3.3b).



(a) Energy per ray. Note that the centre ray has a lower energy and that the outermost ray has a higher energy. (b) Discretized Gaussian irradiance profile.

Figure 3.3: Laser discretization in a regular pattern for a Gaussian beam with radius $R = 3$ mm, laser pulse energy $U_t = 10 \mu\text{J}$ and $N_R = 20$ rings, giving $N = 1261$ initial rays. Adapted from Visser (2011), with permission.

The number of initial rays with N_R rings around a centre ray and $6n$ rays per ring is equal to

$$N = 1 + 3N_R(N_R + 1). \quad (3.8)$$

With a little algebra, it follows that the number of rings required to discretize the beam in at least N rays is equal to

$$N_r = \left\lceil \frac{1}{6} \sqrt{12N - 3} - \frac{1}{2} \right\rceil. \quad (3.9)$$

Preliminary results from Visser (2011) indicate that the regular pattern method is very discretization dependent. This problem was also reported by Cosson et al. (2011), who solved the problem by using a stochastic discretization method. Therefore, a similar approach will be pursued in the following section. The discretization dependence will be discussed further in Chapter 4.

The stochastic method also has the advantage that the number of initial rays does not have to be predetermined before a simulation. In comparison, a major drawback of the regular pattern method is that the number of rays has to be specified beforehand: there is no possibility to obtain representative results when the calculation is aborted prematurely. The implications of this will also be discussed in Chapter 4.

3.2.2 Stochastic beam discretization

In the stochastic approach, each ray has the same initial energy $U = U_t/N$, such that the total energy of all rays equals the total beam energy. The irradiance profile is determined by the ray density distribution in the cross-section of the beam. A Gaussian irradiance distribution is obtained by determining the ray

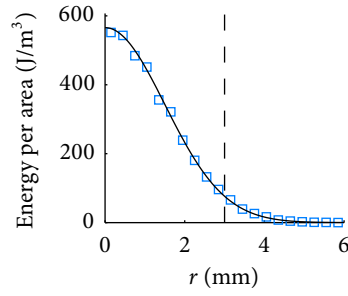


Figure 3.4: Comparison of the radial irradiance of the stochastic laser discretization with the theoretical profile for a beam with radius $R_L = 3$ mm (indicated by the dashed line on the right), laser pulse energy $U_t = 10 \mu\text{J}$ and $N = 10\,000$ initial rays.

origins with two independent stochastic variables with a normal distribution: one for the y -coordinates and one for the z -coordinates:

$$P_x = \frac{1}{R} \sqrt{\frac{2}{\pi}} \exp[-2(x/R)^2], \quad P_y = \frac{1}{R} \sqrt{\frac{2}{\pi}} \exp[-2(y/R)^2], \quad (3.10)$$

where R is again the beam radius. The prefactor ensures that the distributions are normalized.

$$\sum P_x = \int_{-\infty}^{\infty} P_x dx = 1, \quad \sum P_y = \int_{-\infty}^{\infty} P_y dy = 1. \quad (3.11)$$

The x -coordinates of the ray origins are all equal and determined by the focal length and offset (Figure 2.1). Figure 3.2b shows the origin points of 10 000 rays generated with Equation 3.10. In Figure 3.4, the irradiance profile of this discretization is compared to the theoretical profile. Here, we divide the cross-section of the beam into a number of annuli. The irradiance is then found by multiplying the number of rays per annulus by the energy per ray and dividing by the annulus area.

The results of the regular and stochastic discretization method will be compared in Chapter 4, as the following sections will explain further crucial parts of the model.

3.3 REFLECTIONS & REFRACTIONS

To model absorption, the reflections and transmissions of rays are crucial. For each ray, we calculate where it hits the surface of the capillary and derive the direction of transmitted and reflected rays, analogous to Visser (2011). This is described in more detail in Appendix A. The surface of the capillary is assumed smooth, such that only specular reflections occur (Figure 3.5).

The decrease in intensity along each ray is determined with the Lambert–Beer law, as will be discussed in the next section. Still a main question is when to cut off the reflected rays, as part of the rays will reflect infinitely in the capillary. The calculation of further reflections and refractions of a given ray is therefore stopped if the energy at the end the ray falls below a certain threshold (Figure 3.1).

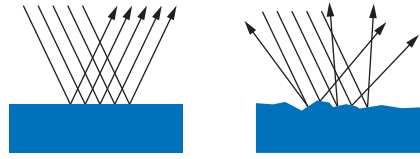


Figure 3.5: Specular (left) versus diffuse reflections. On a smooth surface, a parallel beam of light is reflected as a parallel beam. A rough surface causes reflection in all directions from a macroscopic point of view. Figure adapted from Hecht (2001).

For the stochastic discretization method, where each ray has the same initial energy, this threshold is set at 1/1000 of the initial energy per ray. For the regular pattern discretization method, the threshold is set at 1/1000 of the average initial energy per ray. For rays that are directed towards open space, an end point is determined.

3.4 SPATIAL DISCRETIZATION OF ABSORPTION

We do not have to take into account the variation of volumetric absorption for different wavelengths. If this is required, the analysis of Sun et al. (1999) is a good starting point.

To model absorption, the working liquid is considered to satisfy the Lambert–Beer absorption law:

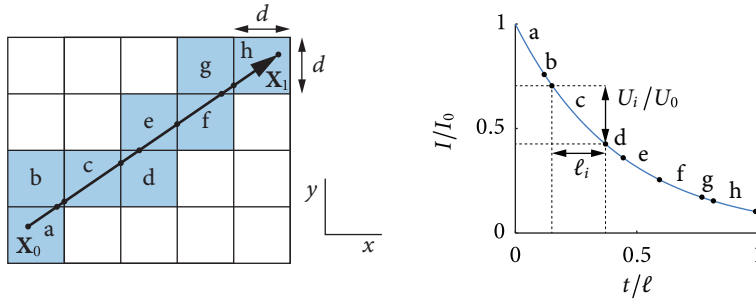
$$\frac{I}{I_0} = 10^{-\alpha \ell}, \quad (3.12)$$

where ℓ is the distance a ray travels through the working liquid with absorption coefficient α , resulting in a ratio I/I_0 of the intensities (or power) of the transmitted and incident light. No scattering is taken into account. To model ink, we use the experimentally determined absorption coefficient $\alpha = 8.4 \times 10^3 \text{ m}^{-1}$. For glass and air, the absorptivity is negligible compared to that of ink, so an absorption coefficient of 0 is assumed.

To obtain a spatial profile of the absorbed energy, space itself is partitioned into a grid of cubic volume cells. To find the cells that each ray encounters and the distance traversed in each cell, the grid is traversed from the begin point \mathbf{X}_0 to the end point \mathbf{X}_1 of the ray with a modified implementation of the voxel traversal algorithm presented by Amanatides and Woo (1987). Here, each ray is described by the equation $\mathbf{X}_0 + t\mathbf{v}$, where \mathbf{X}_0 is the starting point of the ray, \mathbf{v} the direction vector and t the distance travelled along the ray. For example, in the two dimensional case of Figure 3.6a, the ray encounters the cells a, b, c, d, e, f, g and h, in that order, as t increases from 0 to the length ℓ of the ray. The lengths per cell ℓ_i are the distances between intersections of the ray and the grid. These lengths are used to calculate the fractions of energy dissipation per cell U_i/U_0 with the Lambert–Beer law (Figure 3.6b).

Adding up the contributions of all rays for every cell gives the required absorption profile. Since each ray passes through a single material (the boundaries between materials determine the end points of rays and begin points of reflected and refracted rays), the material is treated as a ray property, and not a cell property. That way, no unnecessary calculations have to be made for rays that do not travel through the working liquid.

From the obtained energy distribution, other numerical methods can be used to obtain the resulting temperature profile and cavitation dynamics. For example,



(a) A ray traversing a 2D grid. Adapted from Amanatides and Woo (1987). (b) Absorbed energy per volume element.

Figure 3.6: Spatial discretization of absorption per ray.

Cosson et al. (2011) obtained a temperature distribution from ray tracing results by using the absorbed energy as volumetric source term in the heat balance equation, which was solved with a finite element method. This will be discussed further in Chapter 4 and 5. In the following section, a straightforward approach is used to get a first indication of the cavitation bubble growth.

3.5 ESTIMATION OF BUBBLE VOLUME

To compare the ray tracer output with experimental data, the bubble growth has to be derived from the discretized energy absorption profile. For this purpose, Visser (2011) proposed a simple model, where each volume element in the absorption grid is considered to be instantly vaporized if a threshold energy is exceeded:

$$U_a \geq \underbrace{\rho C_p \Delta T}_{U_b} + \underbrace{\rho \Delta H_{\text{vap}}}_{U_v} \quad (3.13)$$

where U_a is the absorbed energy per unit volume, ρ and C_p the density and heat capacity of the liquid, $\Delta T = T_b - T_i$ is the difference between the boiling temperature and the initial temperature and ΔH_{vap} is the enthalpy of vaporization. The first term on the right hand side, U_b , accounts for heating the liquid up to the boiling point, the second term U_v describes the energy required to evaporate the whole volume. We approximate our 10 % ink solution as pure water with an initial temperature $T_i = 20^\circ\text{C}$, boiling temperature of $T_b = 100^\circ\text{C}$, density $\rho = 1000 \text{ kg m}^{-3}$, heat capacity $C_p = 4.18 \text{ kJ kg}^{-1} \text{ K}^{-1}$ and enthalpy of vaporization $\Delta H_{\text{vap}} = 2257 \text{ kJ kg}^{-1}$. The resulting energy density for bubble formation then becomes 2.59 GJ/m^3 .

However, if we consider discrete volume elements and apply this threshold, the evaporated volume is still underestimated. The method does not take into account elements for which the added energy is more than required to heat the amount of liquid to the boiling point, but not enough to fully evaporate the volume. Only elements that have absorbed enough energy to completely evaporate are considered evaporated. To obtain a better indication of the total evaporated volume, an approach bearing some resemblance to the Volume of Fluid method (VOF) is used. Here, each grid cell is considered to contain two phases, liquid

and vapour. We define the evaporated fraction η as the part of the cell volume that is vapour. While the VOF method use information from neighbouring cells to derive the actual interface, here a straightforward estimation is used, based only on the absorbed energy in each cell:

- $\eta = 0$ if there is no evaporation, when $U_a \leq U_b$;
- $\eta = 1$ if there is complete evaporation, when $U_a \geq U_b + U_v$;
- $\eta = (U_a - U_b)/(U_v - U_b)$ if there is partial evaporation, when $U_a > U_b$ and $U_a < U_b + U_v$.

The total bubble volume V_b is then calculated as the sum of all the evaporated fractions η_i multiplied by the volume per element:

$$V_b = d^3 \sum_i \eta_i. \quad (3.14)$$

Still, an error is introduced at the volume elements near the capillary wall, because the bubble estimation assumes that the volume surrounding a grid point consists of absorbing liquid only, while at the wall part of the volume is not ink but glass. The heating and evaporation will be underestimated, because the energy is spread over a larger volume than the ink actually occupies. This error is decreased by choosing a grid spacing such that a whole number of volume elements fits in the capillary diameter. The remaining error will be neglected here. It can be decreased further by using a finer grid, or removed altogether by calculating the actual volume of liquid per cell.

Both the simple threshold and evaporated fraction method give at best crude approximation of the bubble volume, especially when a coarse grid used. Still, the results give a remarkable qualitative match with experimental results. They will be discussed in the next chapter. The methods may also be used to study how much energy is required to generate cavitation bubbles. [Tagawa et al. \(2012\)](#) used cavitation bubbles to create high-speed jets and observed that below a certain threshold of absorbed energy, no jet was formed. This leads to the question whether a cavitation bubble is still produced or not in that case. Furthermore, the jet speed may be related to the bubble volume. Knowledge on the bubble volume may thus be used to better control such jets.

In this chapter we will evaluate the model developed in the previous chapter. We start with an analysis of the convergence and efficiency, and conclude with a comparison with experiments.

4.1 BEAM DISCRETIZATION CONVERGENCE

For a given spatial grid, a sufficient amount of initial rays is required for a converged absorption profile. This is illustrated in [Figure 4.1](#), which shows slices of the calculated absorption profile in the xy -plane at $z = 0$, the xz -plane at $y = 0$ and a yx -plane. The focal point of the laser (coming from the right) is projected at $x, y, z = 0$. In a–c and e–g, the number of initial rays is insufficient, as the absorption profile changes when the number of rays increases. The profile approaches its final appearance at about 10 000 initial rays for both beam discretization methods.

For regular pattern beam discretization, the profile is always the same for a given number of initial rays. This means that there will be a systematic error until convergence is achieved. This discretization dependence for regular-spaced ray discretization was also reported by [Cosson et al. \(2011\)](#). While the stochastic discretization method also requires a sufficient number of initial rays, the error is now random rather than systematic.

To obtain a quantitative indication of the convergence, two methods were used. These methods circumvent the lack of an analytical result to compare the simulations results with. First, we look at the total absorption for an increasing number of rays. Second, we look at the change in the absorption profile for increasing numbers of rays. The spatial grid resolution was kept constant at $9.5 \mu\text{m}$.

[Figure 4.2a](#) shows the total absorption for increasing numbers of initial rays for both the regular pattern and stochastic beam discretization. From this graph, it appears that the regular discretization converges with a lower number of rays compared to the stochastic method. There also is a slight difference in total absorption. This difference can be explained by the unavoidable difference of the maximum number of rays calculated with each method. In both methods, calculation of reflections and refractions is halted when the energy of a ray is less than $1/1000$ of the average initial ray energy, but the energy per ray is constant for the stochastic method and variable for the regular method.

[Figure 4.2b](#) shows the relative change of the absorption profile, calculated between successive increments of the number of initial rays with 10 000 rays. The relative change ΔU_r in the absorption profile is defined as the sum of the changes in absorbed energy per grid cell, divided by the total absorbed energy:

$$\Delta U_r = \frac{\sum_i |U_i(n) - U_i(n-1)|}{\sum_i |U_i(n)|}, \quad (4.1)$$

where i refers to grid points, and n to successive calculations. To achieve a less than 1 % change, about 100 000 initial rays are required in this configuration.

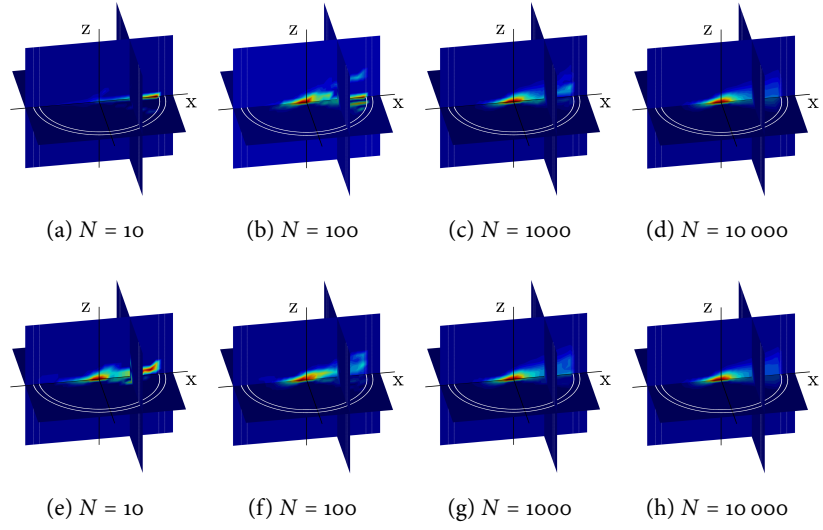


Figure 4.1: Influence of the number of initial rays on the absorption profile for a given spatial grid resolution. The capillary contours are indicated by white lines. The top and bottom row show results from the regular pattern and stochastic beam discretization, respectively.

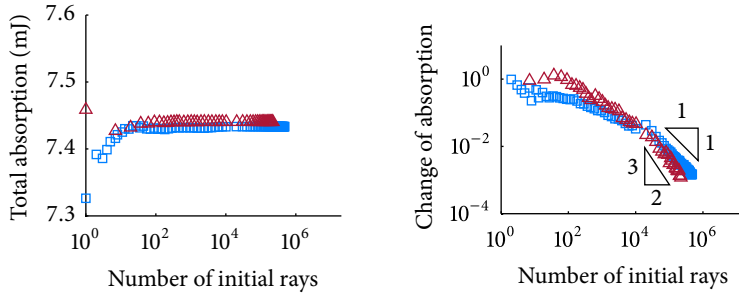
Initially, the change is smaller for the stochastic beam discretization. However, from about 10^4 initial rays, from which the number of initial rays is increased with constant step, the change is smaller for the regular discretization. The slope of the graphs indicate that the error then scales with $1/N$ for the stochastic beam discretization and with $1/N^{3/2}$ for the regular beam discretization.

For increased focal displacement or a finer spatial grid, the required number of initial rays increases. Further analysis is required to determine the dependence of the result on the spatial discretization. To obtain discretization independent results, a converged result is required. For this, we can either define a minimum change in the absorption profile, or introduce a similarity variable. For example, we can define a ray density number as the number of absorbed rays divided by the number of grid cells with nonzero absorption. The usability of such a number requires further investigation.

The varying demands on the number of initial rays favour the stochastic beam discretization method, for this method allows to add initial rays until a certain level of convergence is achieved. The regular method, on the other hand, uses a predetermined number of initial rays, with no possibility to adapt the calculation to the convergence of the result during a simulation.

4.2 EFFICIENCY ANALYSIS

To improve the accuracy and speed of the simulation, the memory and time efficiency of the code was analyzed and improved. The speed of the code was increased up to $200\times$ compared to preliminary code by [Visser \(2011\)](#), which used a different spatial absorption algorithm. Memory limitations for increasing numbers of initial rays were eliminated by calculating rays in batches.



(a) Convergence of the total absorbed energy for an 8 mJ laser pulse. (b) Relative change of the absorption profile.

Figure 4.2: Convergence analysis for increasing numbers of initial rays for a fixed spatial grid with $d = 9.5 \mu\text{m}$ and $x_F = 0$, comparing stochastic (\square) and regular pattern (\triangle) beam discretization.

4.2.1 Time efficiency

Figure 4.3a shows the simulation runtime for an increasing number of initial rays for the two beam discretization method. The slope of 1 in the log-log plot indicates that the simulation runs in linear time with respect to the number of initial rays. The higher computation time for the stochastic method results from the difference in limiting the number of traced rays, which results in a higher number of total rays for a given number of initial rays for the stochastic method (see Section 3.3).

4.2.2 Memory efficiency

Figure 4.3b shows the increase in memory for both beam discretization methods. The regular pattern discretization runs in linear memory, whereas the stochastic almost runs in constant memory. The linear increase of memory limits further increase of the number of rays for the regular method. The lower memory usage of the stochastic methods results from the implementation of a batch processing method and not from the discretization method. For the stochastic method, initial rays were added in batches, while for the regular pattern method, all rays were calculated at once.

4.3 RESULTS

Figure 4.4 shows the model results for varying focal displacement. All other input parameters were matched to the experimental setup (see Appendix B for an overview). The local energy absorption was determined using a grid with $9.5 \mu\text{m}$ spacing and 100 000 initial rays. Here, we compare these simulation results with the experimental results from Chapter 2. A qualitative comparison confirms that a larger volume of fluid is heated for increasing focal offset. Furthermore, the position with the most absorbed energy and its displacement with increasing focal displacement match the experimental trend. In focus, the most energy is deposited near the axis of the tube (Figure 4.4a, see also Figure 2.2a). Displace-

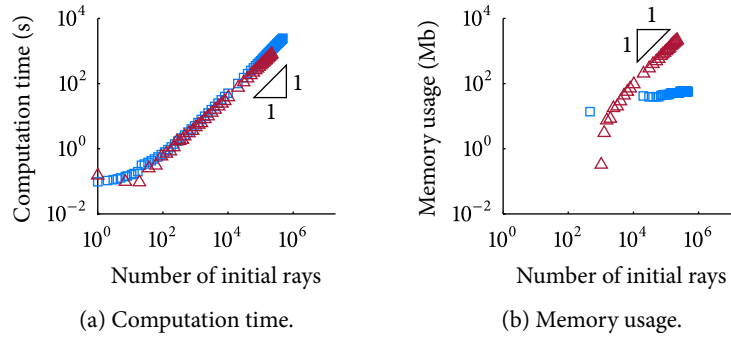


Figure 4.3: Efficiency analysis of the simulation, comparing stochastic (\square) and regular pattern (\triangle) beam discretization.

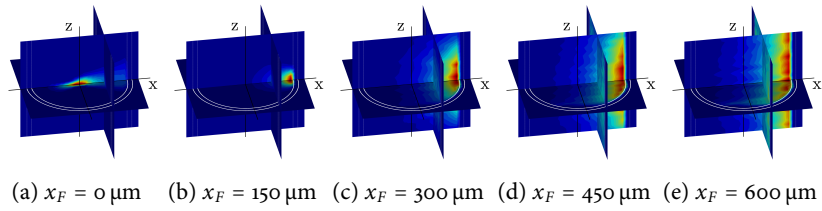


Figure 4.4: Modelled local absorption profile in a $200 \mu\text{m}$ capillary tube for increasing focal displacement x_F towards the laser. The colours show the relative difference within each image.

ment of the focus to the right shifts the absorption pattern towards the edge of the tube (Figure 4.4b–e, see also Figure 2.2b–f).

Figure 4.5 shows the modelled bubble volume for varying focal displacement. Both the results of the simple bubble volume method (where cells are either fully evaporated or not) and the evaporated fraction method (where the cell volume consists of part liquid and part vapour) are shown. There are two laser positions that result in a local maximum of the bubble volume. Moving further out focus from these positions results in a decrease of the bubble to zeros. As discussed in Chapter 2, a plausible explanation for the maximum is a competition between increasing heated volume and decreasing beam irradiance.

Figure 4.6 relates the calculated bubble volume to the total absorbed energy. Here the relative bubble volume for each of the two methods used is defined as the bubble volume divided by the maximum bubble volume for that method. The relative total absorption is the fraction of the total laser pulse energy that is absorbed in the capillary. The total absorption is at an almost constant maximum value while the beam width does not exceed the capillary width. Further out focus, an increasing part of the beam does no longer hit the capillary, resulting in a decline of the total absorption. With the current setup, the maxima in bubble volume are located near the limits of the maximum absorption range.

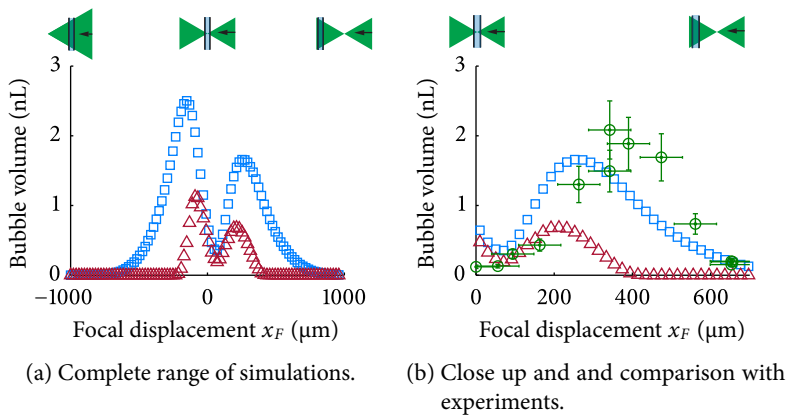


Figure 4.5: Initial bubble volume modelled with the simple bubble threshold method (Δ) and the evaporated fraction method (\square), compared with the experimentally determined volume at $3 \mu\text{s}$ (\circ).

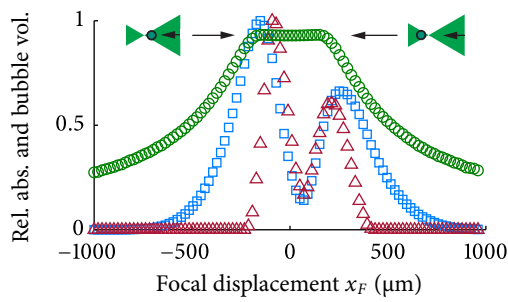


Figure 4.6: Relative total absorption (\circ) and bubble volume determined with the simple bubble threshold method (Δ) and the evaporated fraction method (\square).

4.4 DISCUSSION & CONCLUSION

The simple threshold and evaporated fraction method were used to get an indication of when bubble formation is enhanced or suppressed by estimating the bubble volume. The trend in experimental data fits the modelled trend well within the range of the data.

For the evaporated fraction model, the bubble volume is higher than the simple bubble model. The minimum in the centre is at the same position for both models. However, for the simple model, the position of the maximum and the decline of the volume towards zero are closer to zero. The maximum of the evaporated fraction method agrees better with the experimental results than that of the simple threshold method. Furthermore, the evaporated fraction method almost provides a quantitative match with the experimental data. It has to be noted that this match is rather arbitrary, for a snapshot of the bubble evolution is compared with a single volume indication.

Between the maxima, where the laser is focused on the capillary, the bubble volume reaches a minimum, but not exactly at the projected focal point $x_F = 0$. This shift is presumably due to the geometry of the system. As [Figure 3.1](#) shows,

refractions in the direction of the capillary axis shift the actual focal point away from the laser. A small displacement of the focal position is required to minimize the directly heated volume. This displacement cannot be confirmed with the current experimental results.

The accuracy of the current approach may be improved by using a finer grid. A better comparison with experiments requires that the actual dynamics after the initial energy deposit are captured. This requires more advanced numerical methods that resolve the motion of the liquid/vapour interface of the bubble. While the actual dynamics of bubble formation cannot be resolved with this simple approach, the method still provides results that can be used to enhance cavitation.

CONCLUSIONS & RECOMMENDATIONS

The growth of laser-induced cavitation bubbles in capillary tubes was studied experimentally and numerically. In this final chapter, we summarize the main results and shed light on possible further research.

5.1 EXPERIMENTAL WORK

Experimental results reveal that bubble formation in capillary tubes may be enhanced by a displacement of the focal point of the laser from the capillary axis. This enhancement may be explained by the domination of the increase of the volume directly heated over the decrease of irradiance in a diverging beam.

5.2 NUMERICAL MODELLING

To optimize bubble formation and to improve the understanding of laser-induced cavitation, a numerical model was developed, analogous to preliminary work by [Visser \(2011\)](#). The simulation combines ray tracing of a discretized laser beam (assumed polarized and Gaussian) and spatial discretization of absorption for the resulting rays, assuming a liquid with Lambert–Beer absorption and no scattering. The result is a 3D spatial discretization of local energy deposit. For comparison with experimental results, an energy threshold method was used to obtain an indication for the initial bubble volume.

Compared to the preliminary simulations from [Visser \(2011\)](#), the simulation speed was increased up to 200×, while discretization errors were decreased and accuracy was increased. A key step for this improvement was the implementation of a new algorithm for the spatial discretization of absorption. Furthermore, stochastic discretization of a laser beam provides more flexibility compared to regular pattern discretization previously used.

5.3 RESULTS

The essential features of the experimental results so far are reproduced well with the numerical model. The numerical simulations furthermore predict an optimum location for the focal displacement of the laser. For the application of cavitation, such an optimum focal displacement is a desirable design parameter. With this knowledge, bubble formation may be achieved with less laser power, or enhanced with equal laser power.

5.4 OUTLOOK

The current model requires further numerical and experimental validation. First, the model requires numerical validation for smaller grid sizes. Second, the predicted optimal position of the focal displacement for bubble formation requires experimental validation. Next, there are many more parameters to be

studied, such as the influence of the liquid absorptivity, the capillary diameter, the capillary wall thickness and the laser pulse energy and polarization.

The accuracy of the model could be improved by incorporating the modelling of a finite beam waist (Alda, 2003), scattering (Madsen et al., 1992; Di Ninni et al., 2010) and high-energy absorption (Mansour et al., 1992). Since incorporating these effects would considerably complicate the present model, it is recommended to first estimate the influence of these effects on model output. An extension of the energy threshold model may allow prediction of the bubble position and shape, next to the bubble volume.

The efficiency of the model could be improved by parallel computation and a decrease in grid dimensions, to a volume of interest or by using the symmetry of the setup.

The key motivation to pursue further model development is that the resulting local energy distribution may serve to enhance the initial conditions of computational fluid dynamics models, such as the method developed by Can (2010). Such a coupling may provide further insight into the very early stage of bubble nucleation, which remains a major scientific puzzle.



This appendix describes how a ray incident on a cylindrical bodies is reflected and refracted. We first find whether and where the ray intersects the body and then calculate the direction and amplitude of transmitted and reflected rays for this point of incidence.

A.1 POINTS OF INTERSECTION

Consider a unit cylinder, defined by the equation $x^2 + y^2 = 1$, and a ray with starting point \mathbf{X}_0 , end point \mathbf{X}_1 and direction vector \mathbf{v}_i . The ray can thus be described by the equation $\mathbf{X}_0 + t\mathbf{v}$, with $t \geq 0$. Substituting the x and y components of the ray equation in the cylinder equation and solving for t yields

$$t = \frac{-b \pm \sqrt{b^2 - 4ac}}{2a}, \quad (\text{A.1})$$

where

$$a = v_{i,x}^2 + v_{i,y}^2, \quad b = 2(v_{i,x}X_{0,x} + v_{i,y}X_{0,y}) \quad \text{and} \quad c = X_{0,x}^2 + X_{0,y}^2. \quad (\text{A.2})$$

If there are one or two real solutions, the intersection is given by the smallest non-negative value. If t has no real solution, the ray does not intersect the cylinder. If there are only negatives value, there is an intersection with the line along which the ray travels, but not on the part where the ray is, so here the ray again does not intersect the cylinder.

A.2 DIRECTION OF TRANSMITTED AND REFLECTED RAYS

For a ray incident on an interface between two materials (Figure A.1), the angle of incidence θ_i equals the angle of reflection θ_r , according to the law of reflection:

$$\theta_i = \theta_r. \quad (\text{A.3})$$

For the transmitted ray, the angle of incidence θ_i is related to the angle of refraction θ_r by Snell's law:

$$n_i \sin \theta_i = n_t \theta_t, \quad (\text{A.4})$$

where n_i and n_t are the indices of refraction of the material which the incident and transmitted rays pass through. The incident, reflected and refracted rays all lie in one plane, the so-called plane of incidence.

To determine the path of the rays at a given point of incidence \mathbf{X}_i on a cylinder, we require a vector normal to the cylinder surface. This vector is given by $\mathbf{n} = \mathbf{X}_i/r$, where the radius r of the cylinder acts as normalization constant. The direction of the vector should be opposed to the direction of the incident ray, so it is correct for rays originating outside the cylinder. If the incident ray comes

This appendix is based on unpublished work by Visser (2011), with permission. The analysis follows on a derivation of the transmission and reflections vectors and angles from de Greve (2007).

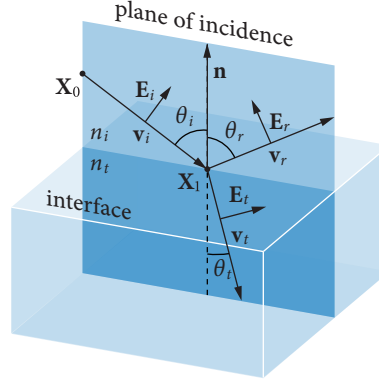


Figure A.1: The incident, reflected and transmitted rays lie in one plane of incidence. \mathbf{n} is the normal vector at the point of incidence, \mathbf{X}_0 and \mathbf{X}_1 indicate the start and end point of the incident ray, \mathbf{v}_i , \mathbf{v}_r and \mathbf{v}_t are the normalized direction vectors of the incident, reflected and transmitted rays, θ_i , θ_r and θ_t are the angles of incidence, reflection and refraction and \mathbf{E}_i , \mathbf{E}_r and \mathbf{E}_t are the electric field vectors of the incident, reflected and transmitted rays. Figure adapted from Hecht (2001).

from inside the cylinder, we use $\mathbf{n} = -\mathbf{X}_1/r$. The direction vectors of the reflected and transmitted rays (\mathbf{v}_r and \mathbf{v}_t) and the angles of incidence and transmission (θ_i and θ_t) can be deduced with vector algebra (de Greve, 2007):

$$\mathbf{v}_r = \mathbf{v}_i - 2(\mathbf{v}_i \cdot \mathbf{n})\mathbf{n}, \quad \mathbf{v}_t = \frac{n_i}{n_t}\mathbf{v}_i - \left(\frac{n_i}{n_t}p + \sqrt{1-q}\right)\mathbf{n}, \quad (\text{A.5})$$

$$\theta_i = \theta_r = |\cos^{-1} p|, \quad \theta_t = |\sin^{-1} \sqrt{q}|, \quad (\text{A.6})$$

where

$$p = |\mathbf{v}_i \cdot \mathbf{n}| \quad \text{and} \quad q = |(n_1/n_2)^2(1-p^2)|. \quad (\text{A.7})$$

If $q > 1$, there is no transmitted ray and complete internal reflection occurs. In this case \mathbf{v}_t has no real solution.

A.3 INTENSITY OF TRANSMITTED AND REFLECTED LIGHT

The fractions of reflected and transmitted light depend on the polarity of the electric field of the incident ray \mathbf{E}_i with respect to the surface of incidence. We therefore define normalized vectors perpendicular and parallel to the surface:

$$\mathbf{n}_\perp = \frac{\mathbf{v}_i \times \mathbf{n}}{|\mathbf{v}_i \times \mathbf{n}|} \quad \text{and} \quad \mathbf{n}_\parallel = \frac{\mathbf{n}_\perp \times \mathbf{v}_i}{|\mathbf{n}_\perp \times \mathbf{v}_i|}. \quad (\text{A.8})$$

We can now decompose the electric field vector into parts normal and parallel to the surface

$$E_{i,\perp} = \mathbf{E}_i \cdot \mathbf{n}_\perp \quad \text{and} \quad E_{i,\parallel} = \mathbf{E}_i \cdot \mathbf{n}_\parallel. \quad (\text{A.9})$$

The magnitude of the electric field from the incident ray is determined from the irradiance (Griffiths (1999)):

$$E_i \approx \sqrt{\frac{2I_i n_i}{\epsilon_i c}}, \quad (\text{A.10})$$

where I_i is the irradiance, n_i the refractive index of the containing material, ϵ_i the vacuum permittivity and c the speed of light. Equation A.10 assumes the magnetic susceptibility is negligible. For visible light in transparent media, such as the current setup, this is usually valid.

If $n_i > n_t$, total internal reflection occurs if $q > 1$. The amplitude coefficients for reflection and transmission then become

$$r_{\parallel} = r_{\perp} = 1 \quad \text{and} \quad t_{\parallel} = t_{\perp} = 1. \quad (\text{A.11})$$

In all other cases, the ray will be partially reflected. The coefficients are then given by the Fresnel equations (Hecht, 2001):

$$r_{\perp} = \frac{n_i \cos \theta_i - n_t \cos \theta_t}{n_i \cos \theta_i + n_t \cos \theta_t} \quad t_{\perp} = \frac{2n_i \cos \theta_i}{n_i \cos \theta_i + n_t \cos \theta_t} \quad (\text{A.12})$$

$$r_{\parallel} = \frac{-n_i \cos \theta_t + n_t \cos \theta_i}{n_i \cos \theta_t + n_t \cos \theta_i} \quad t_{\parallel} = \frac{2n_i \cos \theta_t}{n_i \cos \theta_i + n_t \cos \theta_i}. \quad (\text{A.13})$$

We now combine the decomposed incident amplitude (A.9), the amplitude coefficients (A.11) and (A.13) and the direction vectors (A.8) for the transmitted beams,

$$\mathbf{E}_t = \mathbf{E}_{t,\perp} + \mathbf{E}_{t,\parallel}, \quad \mathbf{E}_{t,\perp} = E_{i,\perp} t_{\perp} \mathbf{n}_{\perp}, \quad \mathbf{E}_{t,\parallel} = E_{i,\parallel} t_{\parallel} \frac{\mathbf{n}_{\perp} \times \mathbf{v}_i}{|\mathbf{n}_{\perp} \times \mathbf{v}_i|}, \quad (\text{A.14})$$

and for the reflected beams

$$\mathbf{E}_r = \mathbf{E}_{r,\perp} + \mathbf{E}_{r,\parallel}, \quad \mathbf{E}_{r,\perp} = E_{i,\perp} r_{\perp} \mathbf{n}_{\perp}, \quad \mathbf{E}_{r,\parallel} = E_{i,\parallel} r_{\parallel} \frac{\mathbf{n}_{\perp} \times \mathbf{v}_i}{|\mathbf{n}_{\perp} \times \mathbf{v}_i|}. \quad (\text{A.15})$$

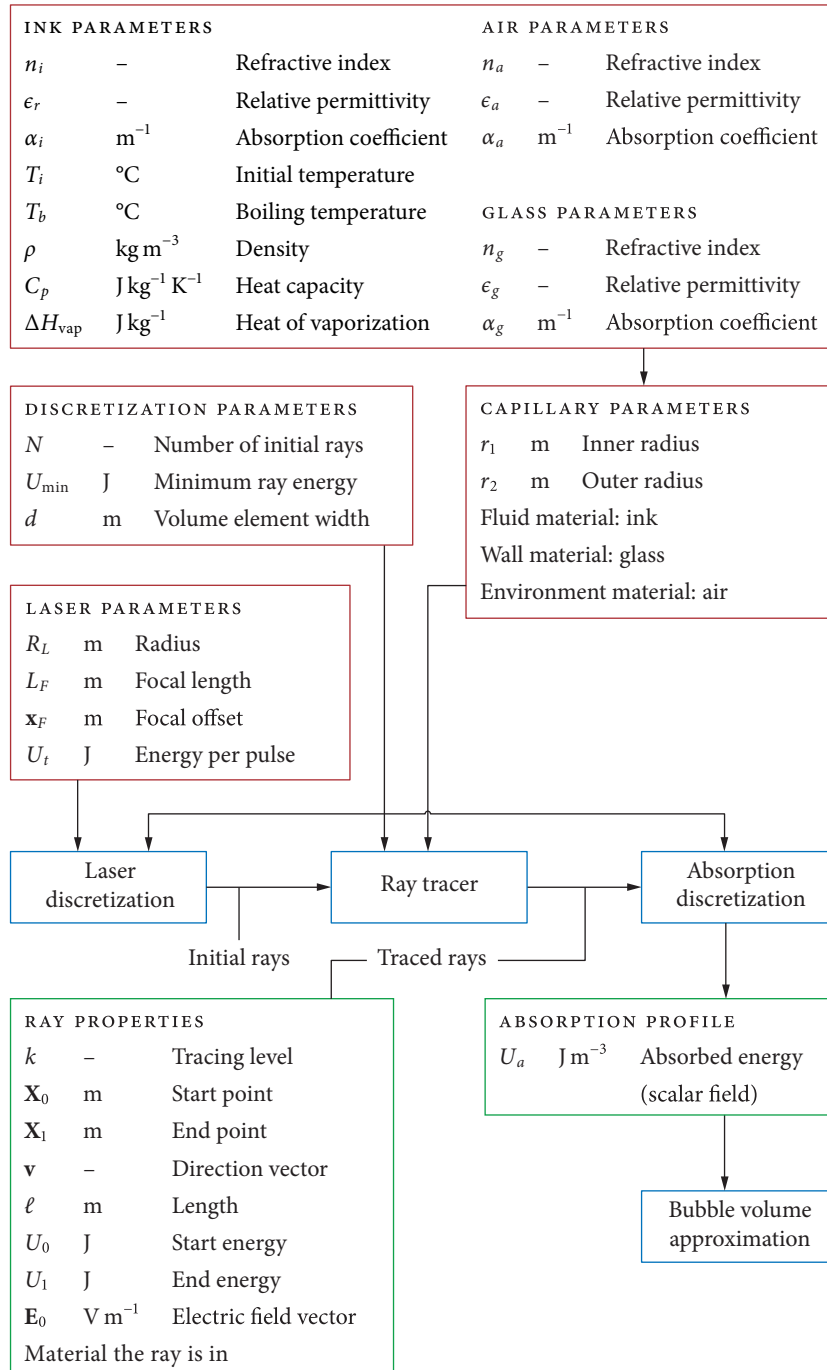
The irradiance of the reflected and transmitted rays become

$$I_r = \left(\frac{|\mathbf{E}_r|}{E_i} \right)^2, \quad I_t = \left(\frac{|\mathbf{E}_t|}{E_i} \right)^2. \quad (\text{A.16})$$

With this analysis, we have fully defined the transmitted and reflected rays for any ray intersecting a cylindrical body.

B

OVERVIEW OF MODEL INPUT & OUTPUT PARAMETERS



BIBLIOGRAPHY

- Alda, J. Laser and Gaussian beam propagation and transformation. *Encyclopedia of Optical Engineering*, p 999–1013, 2003.
- Amanatides, J. and Woo, A. A fast voxel traversal algorithm for ray tracing. In *Eurographics '87*, pp 3–10, 1987.
- Bordival, M., Schmidt, F., Le Maoult, Y., Cosson, B., and Plantamura, B. A ray tracing method to simulate the infrared heating of semi-transparent thermo-plastics. *International Journal of Material Forming*, 3:809–812, 2010.
- Brenner, M. P., Hilgenfeldt, S., and Lohse, D. Single-bubble sonoluminescence. *Reviews of Modern Physics*, 74:425–484, 2002.
- Bringinghurst, R. *The Elements of Typographic Style (version 3.2)*. Hartley & Marks Publishers, 2008.
- Byun, K.-T. and Kwak, H.-Y. A model of laser-induced cavitation. *Japanese Journal of Applied Physics, Part 1*, 43(2):621–630, 2004.
- Can, E. *Vapor Bubbles in Confined Geometries: A Numerical Study*. PhD thesis, University of Twente, 2010.
- Cosson, B., Schmidt, F., Le Maoult, Y., and Bordival, M. Infrared heating stage simulation of semi-transparent media (PET) using ray tracing method. *International Journal of Material Forming*, 4:1–10, 2011.
- de Greve, B. Reflections and refractions in ray tracing, 2007. Retrieved from http://www.bramz.net/data/writings/reflection_transmission.pdf on 16 April, 2012.
- Di Ninni, P., Martelli, F., and Zaccanti, G. The use of India ink in tissue-simulating phantoms. *Optics Express*, 18(26):26854–26865, 2010.
- Felix, M. and Ellis, A. Laser-induced liquid breakdown – a step-by-step account. *Applied Physics Letters*, 19(11):484–486, 1971.
- Garcia, P., Ferriere, A., and Beziau, J.-J. Codes for solar flux calculation dedicated to central receiver system applications: A comparative review. *Solar Energy*, 82(3):189–197, 2008.
- Gonzalez-Avila, S., Klaseboer, E., Khoo, B., and Ohl, C.-D. Cavitation bubble dynamics in a liquid gap of variable height. *Journal of Fluid Mechanics*, 682: 241–260, 2011.
- Greco, V. and Giusfredi, G. Reflection and refraction of narrow Gaussian beams with general astigmatism at tilted optical surfaces: a derivation oriented toward lens design. *Applied Optics*, 46(4):513–521, 2007.
- Griffiths, D. J. *Introduction to Electrodynamics (3rd edition)*. Addison-Wesley, 1999.
- Hecht, E. *Optics (4th edition)*. Addison-Wesley, 2001.
- Lauterborn, W. High-speed photography of laser-induced breakdown in liquids. *Applied Physics Letters*, 21(1):27–29, 1972.
- Lim, K., Quinto-Su, P., Klaseboer, E., Khoo, B., Venugopalan, V., and Ohl, C.-D. Nonspherical laser-induced cavitation bubbles. *Physical Review E*, 81(1), 2010.
- Madsen, S. J., Patterson, M. S., and Wilson, B. C. The use of India ink in tissue-simulating phantoms. *Physics in Medicine and Biology*, 37:985–993, 1992.
- Mansour, K., Soileau, M. J., and Van Stryland, E. W. Nonlinear optical properties of carbon-black suspensions (ink). *Journal of the Optical Society of America B*,

- 9(7):1100–1109, 1992.
- Mitragotri, S. Current status and future prospects of needle-free liquid jet injectors. *Nature Reviews Drug Discovery*, pp 543–548, 2006.
- Nakouzi, S., Pancrace, J., Schmidt, F., Le Maoult, Y., and Berthet, F. Simulations of an infrared composite curing process. *Advanced Engineering Materials*, 13(7):604–608, 2011.
- Ohl, C.-D., Quinto-Su, P., Dijkink, R., Gonzalez, R., Prabowo, F., Huang, X., Wu, T., and Venugopalan, V. Cavitation as a microfluidic tool. In *CAV2009 – 7th International Symposium on Cavitation, 16-20 August 2009, Ann Arbor, MI*, 2009.
- Quinto-Su, P., Lim, K., and Ohl, C.-D. Cavitation bubble dynamics in microfluidic gaps of variable height. *Physical Review E*, 80(4), 2009.
- Sokolov, M. and Saltiel, C. Numerical evaluation of radiation absorption by a fluid confined in a semi-transparent circular cylinder. *Solar Energy*, 27(1): 31–35, 1981.
- Sun, C., Can, E., Dijkink, R., Lohse, D., and Prosperetti, A. Growth and collapse of a vapour bubble in a microtube: the role of thermal effects. *Journal of Fluid Mechanics*, 632:5–16, 2009.
- Sun, Y., Fracchia, F. D., and Drew, M. S. Rendering the phenomena of volume absorption in homogeneous transparent materials. In *The 2nd Annual IASTED International Conference on Computer Graphics and Imaging (CGIM'99)*, pp 283–288, 1999.
- Tagawa, Y., Oudalov, N., Visser, C., Peters, I., van der Meer, D., Sun, C., Prosperetti, A., and Lohse, D. Highly focused supersonic microjets. *ArXiv e-prints*, 1112.2517v4, Apr. 2012.
- van der Bos, A., Zijlstra, A., Gelderblom, E., and Versluis, M. iLIF: illumination by Laser-Induced Fluorescence for single flash imaging on a nanoseconds timescale. *Experiments in Fluids*, 51:1283–1289, 2011.
- Visser, C. Absorption of polarized light by liquid in cylindrical vessels. Sept. 2011.
- Yang, B. and Prosperetti, A. Vapour bubble collapse in isothermal and non-isothermal liquids. *Journal of Fluid Mechanics*, 601:253–279, 2008.
- Zwaan, E., Le Gac, S., Tsuji, K., and Ohl, C.-D. Controlled cavitation in microfluidic systems. *Physical Review Letters*, 98(25), 2007.

ACKNOWLEDGMENTS

Two months ago, I had only barely decided that fluid physics was *the next big thing* for me, and I sent Prof. Detlef Lohse an e-mail, asking for the possibilities of doing a bachelor assignment at Physics of Fluids. The same day, I received four (!) replies with possibilities. Detlef, thank you for this warm welcome, for giving me the chance to develop myself in such an exciting research group and for taking the chair of my bachelor committee.

Of all possibilities, the needle-free injection project immediately drew my attention. I quickly got in touch with Claas Willem, but his initial proposal was not exactly what I was looking for. Luckily, Claas Willem was willing to write an alternative assignment and to supervise me with it. Claas Willem, you found a balance between giving freedom and giving feedback that fit me perfectly. You allowed me to learn from my mistakes on paper and in presentations by analyzing sharply what went wrong. With your attention for detail, I could improve my work further than I could have without. Thank you.

Chao, thanks for taking part in my bachelor committee. Chao, I still remember being somewhat overwhelmed by your enthusiasm when I first met you. I thank you for your encouraging spirit and especially for taking the time to discuss my progress during Claas Willem's vacation.

Miko, I remember lectures where crazy things happened to pianos and where a car of six metres fitted into a garage of five metres – they really inspired me. Your outsider perspective was a great addition to my bachelor committee.

Martijn, Matthea and Claas Willem, you worked with the setup just before I did in a one week project. Thank you for your pioneering work, figuring out the timing of the lasers and the camera and for taking beautiful pictures. The data will be useful for the further validation of the model presented in this thesis.

Erwin, thanks for your help with the validation of my model, and for helping me to create better graphics. Matthijs and Nikolai, I enjoyed working in the student's room with you.

Prof. Andrea Prosperetti, I incredibly enjoyed your ten minute personal lecture on computational fluid dynamics and hope to have more such discussions in the future.

Joanita, without you I would certainly have missed the miniscule window of opportunity for my bachelor defense. And without Gert-Wim, Bas and Martin, I would not have been able to print, which would have made my literature study far more uncomfortable. Thank you.

I thank Robert [Bringhurst \(2008\)](#) for his excellent reference work on typography and André Miede for his classicthesis L^AT_EX template inspired on Bringhurst's work. A postcard is coming soon.

Martijn, Stefan, Daniël (and Boudewijn, Seline and Rogier coaching us), exercising with you this year was a blast! Rowing, cycling, running, crossfit, swimming – a good workout helped me many times to free my mind.

Bart, Elisa, Daniël, Chris, Joost, Sander, thanks for all we shared, from simply drinking coffee to beer games, paint parties and other crazy things that still put a smile on my face. Since we started studying AT our ways have already diverged considerably, but I hope to not lose you out of sight.

Bart, thanks to you I now have an idea of what happens behind the curtains when traffic is redirected. Thank you for going through the trouble of reading my thesis while finishing your own.

And last, but absolutely not least, my family. Jos, Regine, Lianne and Rob, there is nothing like coming home, or *biejt hoes komm'n*. I am grateful for such enduring support and understanding. This thesis would not have been the same without the 'room service' including meat balls and a lot of coffee in the last days of thesis writing.

Martin Klein Schaarsberg
Enschede, June 2012